Title:

Trim41 is essential for preventing X chromosome chaotic synapsis in male mice.

Running Title:

Trim41 is essential for male meiosis

Author Line:

Seiya Oura[1,2], Toshiaki Hino[3], Takashi Satoh[4,5,6], Taichi Noda[1,7,8], Takayuki Koyano[9], Ayako Isotani[1,10], Makoto Matsuyama[9], Shizuo Akira[5,6], Kei-ichiro Ishiguro[11], and Masahito Ikawa[1,2,12,13, *]

Author Affiliations:

[1] Research Institute for Microbial Diseases, Osaka University, Osaka, Japan

[2] Graduate School of Pharmaceutical Sciences, Osaka University, Osaka, Japan

[3] Department of Biological Sciences, Asahikawa Medical University, Asahikawa, Japan

[4] Department of Host Defense, Research Institute for Microbial Diseases, Osaka University, Osaka, Japan.

[5] Laboratory of Host Defense, WPI Immunology Frontier Research Center, Osaka University, Osaka, Japan.

[6] Department of Immune Regulation, Graduate School of Medical and Dental Sciences, Tokyo Medical and Dental University, Tokyo, Japan

[7] Priority Organization for Innovation and Excellence, Kumamoto University, 2-39-1

Kurokami, Chuo-ku, Kumamoto 860-8555, Japan

[8] Division of Reproductive Biology, Institute of Resource Development and Analysis, Kumamoto University, Kumamoto, Japan

[9] Division of Molecular Genetics, Shigei Medical Research Institute, Okayama, Japan

[10] Division of Biological Science, Graduate School of Science and Technology, Nara Institute of Science and Technology, Nara, Japan

[11] Department of Chromosome Biology, Institute of Molecular Embryology and Genetics (IMEG), Kumamoto University, Kumamoto, Japan

[12] The Institute of Medical Science, The University of Tokyo, Minato-ku, Tokyo, 108-8639, Japan

[13] Center for Infectious Disease Education and Research (CiDER), Osaka University, Osaka, Japan

ORCID identifier: 0000-0002-7606-732X for S.O., 0000-0002-8868-5782 for T.S., 0000-0003-0260-7861 for T.N., 0000-0003-1675-2525 for T.K., 0000-0002-4720-2318 for A.I., 0000-0003-2606-059X for M.M, 0000-0002-7515-1511 for K.I., and 0000-0001-9859-6217 for M.I.

[*]**Corresponding Author**:

Masahito Ikawa

Research Institute for Microbial Diseases, Osaka University, Osaka, Japan

+816-8379-8375

ikawa@biken.osaka-u.ac.jp

Keywords:

Meiosis, Synapsis, XY body, Mouse, TRIM41

Summary statement

Trim41-disruption caused abnormal synapsis configuration of the X chromosome and complete infertility in male mice. Thus, TRIM41 prevents the sex chromosome from chaotic synapsis.

Abstract

Meiosis is a hallmark event in germ cell development that accompanies sequential chromosome events executed by numerous molecules. Therefore, characterization of these factors is one of the best strategies to clarify the mechanism of meiosis. Here, we report tripartite motif-containing 41 (TRIM41), a ubiquitin ligase E3, as an essential factor for proper meiotic progression and fertility in male mice. *Trim41* KO spermatocytes exhibited synaptonemal complex protein 3 (SYCP3) overloading, especially on the X chromosome, showing extensive self-synapsis of X chromosome and non-homologous synapsis between the X chromosome and autosomes. Furthermore, the mutant mice lacking the RING domain of TRIM41, required for the ubiquitin ligase E3 activity, phenocopied *Trim41* KO mice. We then examined the behavior of mutant TRIM41 (ΔRING-TRIM41) and found that ΔRING-TRIM41 accumulated on the chromosome axes with overloaded SYCP3. This result showed that TRIM41 exerts the function on the chromosome axes. In summary, our study revealed that *Trim41* is essential for preventing SYCP3 overloading and chaotic synapsis of the X chromosome, suggesting a TRIM41-mediated mechanism for regulating unsyapsed axes during male meiotic progression.

Main text

Introduction

Tripartite motif (TRIM) family proteins consist of more than 70 members in humans and mice (Ozato et al., 2008; Rajsbaum et al., 2014; Versteeg et al., 2013) (also according to NCBI and MGI databases). They contain three zinc-binding domains in the N-terminus: a RING finger domain, one or two B-Boxes (B1/B2) motifs, and a coiled-coil (CC) region (Fig 1A). The RING domains of many TRIM family members have been shown to confer E3 ubiquitin ligase activity (Hatakeyama, 2017; Rajsbaum et al., 2014) (Fig 1B) and implicated in various biological functions such as innate immunity and carcinogenesis regulation (Lassot et al., 2018; Zhang et al., 2013; Zhang et al., 2021). TRIM41-mediated ubiquitination also functions in natural immunity via target protein degradation, including B cell leukemia/lymphoma 10 (BCL10) (Yu et al., 2021), nucleoproteins of the influenza A virus, and vesicular stomatitis virus (Patil et al., 2020; Patil et al., 2018). Therefore, to examine the defects in natural immunity, we produced *Trim41* knockout (KO) mice. However, unexpectedly, *Trim41* KO male mice exhibited complete infertility due to meiotic defects. Thus, we focused on the analysis of meiotic events in this report.

Here, meiosis is a hallmark event in germ cell development when homologous chromosomes undergo the physical juxtaposition (called synapsis) and shuffling of genetic material via a process known as homologous recombination. Upon entry into meiosis, in the leptotene stage, programmed DNA double-strand breaks (DSBs) are introduced (Keeney et al., 2014) and enable genome-wide search for homology through

the repair process, although a significant amount of chromosome pairing occurs before the initiation of DSBs (Boateng et al., 2013). This homologous search drives the pairing and alignment, finally leading to the synapsis of all homologs in the pachytene stage. However, unlike autosomes that fully synapse between homologs, sex chromosomes (X and Y in most mammals) have only synapsed at the pseudoautosomal region (PAR) and sequestered into a physically separated nuclear territory known as the XY body. The molecules involved in these complex chromosome events are not fully characterized yet, especially in mammals, due to difficulties in culturing and genetically manipulating spermatogenic cells *in vitro*. Thus, physiological screening with KO mice has been a powerful strategy to identify meiosis-related factors (Gray and Cohen, 2016; Oji et al., 2020; Oura et al., 2021).

In this study, we revealed that *Trim41* deficiency cause synaptonemal complex protein 3 (SYCP3) overloading on several chromosome axes. Among them, the X chromosome was mainly affected, exhibiting aberrant synapsis with autosomes rather than forming the XY body. A transgene with a germ cell-specific expression rescued the spermatogenesis defects, which showed that TRIM41 directly regulates meiosis. Further, deletion of the RING domain (ΔRING) phenocopied *Trim41* KO. More importantly, ΔRING-TRIM41 accumulated on chromosome axes with overloaded SYCP3, suggesting that TRIM41-mediated protein degradation may act for removing overloaded SYCP3. Thus, our study demonstrated that mammalian spermatocytes have a TRIM41-mediated mechanism for preventing sex chromosome chaotic synapsis.

Results

Trim41 is evolutionarily conserved between mammals and highly expressed in pachytene germ cells.

The Treefam database (http://www.treefam.org/; Release 9, March 2013) shows that TF342569, a family containing TRIM41, has been annotated in 50% of eukaryotes, 98 % of vertebrates, and 100% of mammals (Fig. S1A). Also, phylogenetic analysis with Clustal W2.1(Larkin et al., 2007) showed that TRIM41 was highly conserved in many mammals, including cattle, dogs, mice, and humans (Figs 1C and S1B). Next, to determine the expression profile of *Trim41*, we performed RT-PCR using cDNA obtained from adult tissues, postnatal testis, and embryonic ovary. These RT-PCR showed that *Trim41* is expressed ubiquitously (Figs 1D–1F), albeit the most highly in testis (Fig. 1D). Furthermore, according to published single-cell RNA-sequencing (scRNA-seq) data analyzing mouse testis (Hermann et al., 2018) and embryonic ovary (Niu and Spradling, 2020), *Trim41* was the most highly expressed in pachytene germ cells (Figs S1C and S1D). These results suggest that TRIM41 functions during the meiotic phase of mammalian gametogenesis.

Trim41 is essential for male fertility

To uncover the function of *Trim41 in vivo*, we generated *Trim41* KO mice by transfecting embryonic stem cells (ESCs) with a targeting vector (Fig. 1G; vector). Targeted ESC clones were injected into ICR embryos to obtain chimeric mice. The chimeric mice were mated with wild-type (WT) females to establish *Trim41* KO lines (Fig. 1H). KO mice obtained by heterozygous intercrosses showed no overt gross defects in development, behavior, and survival. Then, we housed individual *Trim41* KO male mice

with wild type (wt) females for two months to analyze their fertility. Although we observed 19 vaginal plugs, *Trim41* KO males failed to sire pups (Fig. 1I). On the other hand, we obtained pups from the mating pair of *Trim41* KO females and *Trim41* Het males (7.4±2.3; Fig. 1J), indicating that *Trim41* is dispensable for female fertility. As *Trim41* Het male mice are fully fertile, we used littermate heterozygous males as controls in some experiments.

A transgene under *Clgn* promoter restored infertility of *Trim41* KO males

To confirm infertility phenotype of *Trim41* KO males was due to *Trim41* deficiency, not an aberrant genetic modification near the *Trim41* locus, and rule out the possibility that latent systemic abnormalities affected male fertility, we carried out a tissue-specific rescue experiment by generating transgenic (Tg) mouse lines. First, we injected a DNA construct having PA-1D4-tagged *Trim41* under the testis-specific Clgn promoter (Watanabe et al., 1995) (Fig. 1G; Tg) and established a Tg line (Fig. 1H; Fw2-Rv3). *Clgn* promoter-driven *Trim41* expression started around postnatal day (PND) 9–11 (Fig. S2A), corresponding to the spermatocyte appearance. The Tg expression was also confirmed by immunoblotting analysis using anti-PA (Fig. S2B) and -TRIM41 antibody (Fig. S2C), although the expression level of Tg was lower than that of intrinsic *Trim41* (Fig S2C; WT v.s. KO-Tg). Then we housed *Trim41* KO male mice expressing the Tg (referred to as KO-Tg) with WT females and observed the normal count of pups (Fig. 1I), showing the *Clgn* promoter-driven *Trim41* Tg rescued the fertility of KO males. These results indicated that *Trim41* expression from meiotic entry onward in testis is essential for male fertility.

166 **_Trim41_ KO male mice exhibited oligozoospermia**

167 When we observed gross testis morphology, *Trim41* KO testes were smaller
168 than those of control (testis/ body weight: 3.2±0.3 x 10^{-3} [WT], 3.2±0.2 x 10^{-3}
169 [Het],1.2±0.2 x 10^{-3} [KO]; Figs 2A and 2B), indicating defective spermatogenesis in
170 *Trim41* KO testis. To define the cause of testicular atrophy, we performed hematoxylin
171 and periodic acid-Schiff (HePAS) staining of testicular sections. While three germ cell
172 layers existed in control testis sections, only two layers of germ cells existed in *Trim41*
173 KO testis (Fig. 2C; low magnification). The number of spermatocytes and spermatids
174 dramatically decreased in the KO testis (Fig. 2C; stage VII–VIII and XII). Although a few
175 elongating/elongated spermatids existed in the KO testis, their nuclei were not fully
176 compacted (Fig. 2C; red arrows). Consistent with the dramatic decrease of
177 spermatocytes and spermatids, the number of TUNEL positive cells increased in KO
178 testis compared with Het counterparts (Figs 2D and 2E). The TUNEL positive cells were
179 frequently observed in the second layer (Fig. 2D; high magnification). We did not see
180 the accumulation of TUNEL positive cells in a specific stage of the seminiferous
181 epithelium cycle (Fig. 2E). These results showed that spermatocytes after the
182 pachytene stage were gradually eliminated by apoptosis. As a result, only a few mature
183 spermatozoa existed in the cauda epididymis (Fig. 2F). In addition, all the spermatozoa
184 exhibited abnormal head/tail shapes (Fig. 2G) and were immotile. These *Trim41* KO
185 spermatogenesis defects were restored by *Clgn-Trim41* (Figs 2A–2F), albeit partially in
186 TUNEL analysis (Fig 2F). These observations suggested that *Trim41* KO males
187 exhibited spermatogenesis defects, leading to oligozoospermia.
188
189 **_Trim41_ KO spermatocytes underwent SYCP3 overloading**

Due to an apparent defect during meiosis, we examined DNA DSBs and synapsis by immunostaining surface chromosome spreads with anti-γH2AX and SYCP3, respectively (Figs 3A and 3B). The SYCP3/γH2AX immunostaining pattern in leptotene and zygotene spermatocytes was comparable between the two genotypes, showing that *Trim41* KO spermatocytes underwent programmed DSBs and initial assembly of the synaptonemal complex. However, the compaction of the XY axes, a telltale signature of XY body formation, was rarely observed in KO spermatocytes (Figs 3B and 3C). Consistent with the XY body malformation, the pachytene and diplotene populations decreased dramatically in KO testis (Fig. 3D). More strikingly, intense SYCP3 signals were observed on both autosomes and sex chromosomes (Figs 3B and 3C). The autosomes with the overloaded-SCYP3 tended to be inside of γH2AX signals, suggesting that the overloading of SCYP3 correlates with autosome unsynapsis. Furthermore, we also observed multilayer SCYP3 axes in the X chromosome (Fig. 3C; yellow arrowhead) and juxtaposition of sex chromosome and autosomes (Fig. 3C; red arrowhead). Such overloading of SYCP3 became evident once homolog synapsis had completed at pachytene rather than at zygotene/pachytene transition (zygotene/pachytene transition; Figs S3A and S3B).

Since localization of axial element proteins, SYCP2 and SYCP3, depends on cohesin axial core that is generated by REC8 and RAD21L (Fujiwara et al., 2020; Ishiguro et al., 2014; Ishiguro, 2019), we examined the REC8 and RAD21L in *Trim41* KO spermatocytes. Consistent with SYCP3 overloading, REC8 and RAD21L tended to be hyperaccumulated (Fig. S4). Although RAD21L gradually dissociates from axial elements from late pachytene onwards in WT spermatocytes (Fig. S4C) (Ishiguro et al., 2011), the dissociation was evident in early pachytene of KO spermatocytes (Fig. S4D).

This observation is at least in part consistent with the evidence that Trim41 is co-immunoprecipitated by RAD21L (Fujiwara et al., 2020).

Interestingly, the overloaded SYCP3 remained on a few chromosomes even in metaphase I and anaphase I (Fig .3E; blue arrowheads). Further polycomplex-like structure, aggregate of SYCP3, was also observed apart from chromosomes (Fig .3E; magenta arrowheads). In addition, some chromosomes connected with the SYCP3 failed to align in the equatorial plate (Fig. 3E; Metaphase I) and were left behind between two centrosomes (Fig. 3E; Anaphase I). Probably because of the remained SYCP3 axes, one or two chromosomes failed to form bivalents and remained as univalents at metaphase I (Fig. 3F). Because chromosome alignment requires a tension across homologs during metaphase I (Kim et al., 2015; Woods et al., 1999), it was likely that lack of chiasmata caused misalignment of those univalents. These results showed that the SYCP3 amount on chromosome axes and synapsis configuration was misregulated in *Trim41* KO spermatocytes.

SYCP3 overloading were biased to the X chromosome

Then, to examine whether SYCP3 overloading is biased to specific chromosomes, we combined SYCP3 immunostaining with multicolor fluorescence in situ hybridization (mFISH; Fig. 3G). The X chromosomes showed more frequent SYCP3 overloading than autosomes (Fig. 3H; X chromosome: 37 out 43 cells; autosome: 12 out 43 cells). Of note, the autosomes with overloaded SYCP3 signals were almost random (Fig. 3H). Finally, we examined the pachytene stage in the E15.5 female ovary. The gross gonad morphology was comparable between the two genotypes (Fig. S5A). The SYCP3 overloaded axes were observed only in a few germ cells (Fig. S5B). This result

was contrast to the observation that SYCP3 overloading was frequent on X chromosome in spermatocytes (Fig. 3H). As a result, folliculogenesis progressed normally (Fig. S5C), and *Trim41* KO female mice were fully fertile (Fig. 1M). Overall, these results showed that *Trim41* is essential for the proper behavior of the unsynapsed X chromosome.

SYCP3 overloaded X chromosome saw self- and non-homologous- synapsis.

Next, to examine the synapsis state, we visualized the central element of the synaptonemal complex (synapsed axes; Figs 4A and 4B) and unsynapsed axes (Figs 4C and 4D) by immunostaining surface chromosome spreads with anti- SYCP1 and BRCA1 antibodies, respectively. SYCP1 is a molecule known to localize between the lateral element of the synaptonemal complex of homologous chromosomes and form transverse filaments, rungs of a ladder of synapsis (Liu et al., 1996; Meuwissen et al., 1992). BRCA1, the product of the breast cancer 1, accumulates on unsyapsed axes of sex chromosomes (Scully et al., 1997). Consistent with Fig. 3C (indicated by a red arrow), X chromosome and autosome were connected by SYCP1 (Fig. 4B; white arrow) in some spermatocytes. SYCP1 signals tended to remain on the overloaded SYCP3 of X chromosomes (Fig. 4B), indicating that the X chromosomes synapse by themselves or between sister chromatids. Strikingly, we observed multilayered SCYP1 signals in some spermatocytes (Fig. 4B; blue arrows).

On the other hand, the BRCA1 staining pattern became uneven throughout the X chromosomes (Fig. 4D; yellow and red arrows), indicating that the X chromosomes have synapsed somehow. Furthermore, BRCA1 was positive on several autosomes with overloaded SYCP3, suggesting that meiotic silencing of unsynapsed chromatin

(MUSC) was activated presumably as a result of delayed homolog synapsis at the SYCP3-overladed region. (Fig. 4D; green arrows). More notably, we observed the BRCA1 negative interface between the X chromosome and autosome axes (Fig. 4D; red arrow), suggesting that the X chromosome synapses with the autosome. These results indicated the X chromosome synapsed by themselves or with autosomes in *Trim41* KO spermatocytes.

$Trim41^{\Delta RING/\Delta RING}$ male mice phenocopied $Trim41^{neo/neo}$ male mice.

To examine whether the RING domain is essential for *Trim41* function, we disrupted the RING domain by inserting the HA affinity tag sequence (Fig. 5A; referred to as ΔRING). The ΔRING-TRIM41 loses only ubiquitin ligase activity, not interaction with target proteins (Patil et al., 2020; Patil et al., 2018). We microinjected two gRNA/Cas9 ribonucleoprotein complexes and a ssODN into zygotes (Fig. 5A). Of 145 injected eggs, 119 eggs reached the two-cell stage. Then we transplanted the two-cell eggs into the oviducts of six pseudopregnant female mice and obtained twenty-five pups. The genotype PCR screening (Fig. 5B) detected the intended mutation with a 180 bp deletion and HA tag insertion (referred to as $Trim41^{\Delta RING}$) from ten pups. Immunoblotting analysis with anti-HA and -TRIM41 antibodies detected HA-tagged ΔRING-TRIM41 expression (Figs 5C and 5D). Then, we caged $Trim41^{\Delta RING/\Delta RING}$ (referred to as ΔR-Homo; $Trim41^{wt/\Delta RING}$: referred to ΔR-Het) male mice with WT females for two months to analyze their fertility. Although we confirmed 38 vaginal plugs, *Trim41* ΔR-Homo males failed to sire any pups (Fig. 5E) as well as *Trim41* KO males. Further, testis of *Trim41* ΔR-Homo males was smaller than the ΔR-Het counterparts (Figs 5F and 5G) due to spermatogenesis defects (Fig. 5H). The TUNEL-positive cells were

frequently observed in the 2nd layer of tubules (Fig. 5I). Also, TUNEL signals were positive in overall seminiferous epithelial cycles (Fig. 5J). As a result, almost no fully-matured spermatids existed in the cauda epididymis of ΔR-Homo males (Fig. 5K). These results showed that *Trim41*$^{\Delta RING/\Delta RING}$ male mice exhibited the same phenotype as *Trim41*$^{neo/neo}$ male mice, suggesting that the RING domain is essential for TRIM41 function.

ΔRING-TRIM41 accumulated on SYCP3-overlaoded region

Immunostaining analysis with anti-SYCP3 and γH2AX antibodies demonstrated XY body malformation and SYCP3 overloading in ΔR-Homo pachytene spermatocytes (Figs 6A and 6B). Also, the number of pachytene and diplotene spermatocytes decreased dramatically in ΔR-Homo testis (Figs S6A–C). These results corroborated the necessity of the RING domain in TRIM41 functions.

Next, to determine TRIM41 localization, we stained the spread nuclei with an anti-HA antibody (Figs 6C–F). In ΔR-Het spermatocytes, we observed only faint signals throughout the nuclei (Fig. 6C). However, surprisingly, ΔR-Homo spermatocytes saw intense HA signals on the SYCP3-overloaded regions (Figs 6D and S6A; white arrows). The strong HA signals appeared after the zygotene–pachytene transition (Figs S7A). In addition, the HA signals tended to become stronger during prophase I progression (Figs S7A), showing a correlation with SYCP3 overloading. The HA foci were also detected in *Trim41*$^{neo/\Delta RING}$ spermatocytes (Fig. 6E), demonstrating that the removal of the RING domain changed the immunostaining pattern, not the protein level difference. On the other hand, we did not detect the HA immunostaining signals in *Trim41* KO spermatocyte with SYCP3 overloading (Fig. 6F), ruling out the possibility of antibody

cross-reaction. Furthermore, we confirmed the same phenomena in immunostaining analysis with an anti-TRIM41 antibody (Figs S7B–E). These observations showed that ΔRING-TRIM41 accumulated on the SYCP3-overloaded regions, suggesting that TRIM41 functions on the chromosome axes. As a side note, we also identified several HA foci outside of the chromosome axes in zygotene and early pachytene spermatocytes (Figs 6D and S7A; blue arrows), although we could not specify the location of those foci.

ΔRING-TRIM41 accumulated on the synapsed part of the X chromosome.

Finally, we examined the relationship between ΔRING-TRIM41 accumulation and the synapsis state by SYCP1 and BRCA1 immunostaining. First, we confirmed SYCP1 tended to remain on the sex chromosome axes in ΔR-Homo spermatocytes and KO spermatocytes, although the sex chromosome SYCP1 axes were uneven (Figs. 6G and S8A). Then, we compared the SYCP1 immunostaining pattern with the ΔRING-TRIM41 accumulation pattern and noticed that the boundary of the SYCP1 positive and negative parts were hotspots of ΔRING-TRIM41 accumulation (Figs. 6G and S8A; magenta arrowheads). More strikingly, the ΔRING-TRIM41 also existed on the interface between the X chromosome and autosomes (Figs. 6G and S8A; yellow arrowheads). On the other hand, in BRCA1/HA immunostaining analysis, we observed ΔRING-TRIM41 on the BRCA1 negative part of the X chromosome axes (Figs. 6H and S8B; yellow arrowheads). Above all, these observations suggested that ΔRING-TRIM41 accumulated on the synapsed part of the X chromosome axes, and therefore TRIM41 is essential for preventing the chaotic X chromosome synapsis.

333 Given that TRIM41 confers ubiquitin ligase E3 activity (Patil et al., 2020; Patil et
334 al., 2018), we tried to identify the substrates by immunoprecipitation. However, we could
335 not detect SYCP3 in co-IPed elute samples by immunoblotting (Figs S9A–S9F). Also,
336 we could not find candidate proteins in IP-Mass analysis (Figs S9G–S9I). Thus,
337 substrate discovery would be the feature research.

Discussion

In this research, we produced *Trim41* KO mice and analyzed the phenotype. Unexpectedly, *Trim41* deficiency caused meiosis defects and infertility in male mice. The infertility was rescued by a transgene driven by a testis-specific *Clgn* promoter. In detailed analyses, we found that *Trim41* KO spermatocytes exhibited SYCP3 overloading. We also noticed that and the X chromosomes underwent self- and non-homologous- synapsis. Furthermore, we removed the RING domain of TRIM41 (ΔRING) to examine the necessity of the RING domain and found that *Trim41*$^{\Delta RING/\Delta RING}$ phenocopied *Trim41*$^{neo/neo}$ (i.e., KO). Surprisingly, the ΔRING-TRIM41 accumulated on the SYCP3-overloaded regions. The ΔRING-TRIM41 accumulation also correlated with the chaotic X chromosome synapsis.

The most striking phenotype of *Trim41* KO spermatocytes was SYCP3 overloading. In addition, some X chromosomes exhibited multilayered SYCP3 signals, clearly demonstrating self-synapsis of the X chromosome. Although we could not specify, this self-synapsis might be inter-sister synaptonemal complex assembly like those found in REC8 KO spermatocytes (Ishiguro et al., 2014; Ishiguro and Watanabe, 2016; Xu et al., 2005). However, given that we also observed multilayer SYCP1 signals in the X chromosome, we should also consider the possibility of extensive heterologous self-synapsis like those seen in domestic dog pachytene spermatocytes (Federici et al., 2015). The latter possibility is corroborated by another outstanding phenotype of the non-homologous synapsis between the X chromosome and autosomes. Further studies are needed to determine the relationship between these two phenotypes (i.e., SYCP3 overloading and abnormal synapsis configuration; causal relationship or simultaneous

362 phenomena) and whether these phenotypes are direct influences of TRIM41 deficiency
363 or compensatory changes.
364
365 To examine which chromosomes exhibited SYCP3 overloading in *Trim41* KO
366 spermatocytes, we performed multicolor FISH combined with SYCP3 immunostaining
367 and found that the X chromosome was mainly affected. On the other hand, autosomes
368 saw fewer SYCP3 overloading and no biases to specific chromosomes. A possible
369 reason for the X chromosome bias is the unsynapsed nature during the pachytene
370 stage. This inference agrees that only a tiny population of germ cells underwent SYCP3
371 overloading in *Trim41* KO females, whose X chromosomes are fully synapsed during
372 prophase I progression. Therefore, *Trim41*-deficient XO meiosis might be an intriguing
373 future consideration.
374
375 To examine the molecular function of TRIM41, we also produced
376 *Trim41*$^{\Delta RING/\Delta RING}$ mice by replacing 2–61 aa residues with HA-tag sequence, and we
377 found that the HA immunostaining signals on overloaded-SYCP3 region. As the HA
378 signals appeared only when the cells had no functional TRIM41 (i.e. *Trim41*$^{\Delta RING/\Delta RING}$ or
379 *Trim41*$^{neo/\Delta RING}$), we concluded that ΔRING-TRIM41 accumulated on the
380 SYCP3-overloaded regions. This observation suggested that ΔRING-TRIM41 kept
381 targeting the unubiquitinated substrates, and therefore TRIM41 exerts its ubiquitin
382 ligase E3 activity on the chromosome axes. However, we could not narrow down the
383 substrate candidate by IP-Mass analysis. Also, we did not see the interaction between
384 TRIM41 and SYCP3. As the weak/transient binding between enzymes and substrates
385 tends to be challenging to capture in IP analysis (Trinkle-Mulcahy, 2019), the recently

386 developed proximity-dependent biotin identification (BioID) technique (Kim et al., 2016;
387 Roux et al., 2012) could be a future consideration in substrate identification.
388
389 In summary, our result showed that *Trim41* is essential for preventing SYCP3
390 overloading and X chromosome chaotic synapsis. Further studies for substrate
391 identification will unveil the exact molecular functions of TRIM41 and the mechanism for
392 safeguarding X chromosome chaotic synapsis in male meiosis.

Material & methods

Animals

All animal experiments were approved by the Animal Care and Use Committee of the Research Institute for Microbial Diseases, Osaka University (#Biken-AP-R03-01-0). Animals were housed in a temperature-controlled environment with 12 h light cycles and free access to food and water. B6D2F1 (C57BL/6 × DBA2; Japan SLC, Shizuoka, Japan) mice and ICR (SLC) were used as embryo donors; B6D2F1 were used for mating and wild-type control; C57BL6/N (SLC) mice were used to collect RNA for cloning.

Generation of Trim41 KO mice

Trim41 KO mice were generated by transfecting EGR-G101 (Fujihara et al., 2013) with a targeting vector. Then, potentially targeted ES cell clones were selected with neomycin. Correctly targeted ES cell clones and germ-line transmission were confirmed via PCR using primers (GeneDesign, Osaka, Japan) listed in Table S1. Finally, the heterozygous KO mice were mated with B6D2F1 and then maintained by sibling mating. The B6D2 KO mouse line is available from the Riken BioResource Center (Riken BRC, Tsukuba, Japan; #11261) and the Center for Animal Resources and Development, Kumamoto University (CARD, Kumamoto, Japan; #3019).

Generation of Trim41 transgenic mice

The mouse *Trim41* cDNA (ENSMUST00000047145) tagged with PA and 1D4 was inserted under the control of the mouse Clgn promoter (Addgene #173686) (Ikawa et al., 2001; Watanabe et al., 1995). The *Trim41* cDNA inserted plasmids are deposited

417 at Riken BRC and Addgene. After linearization, the DNA construct (2.16 ng/μL; 0.54
418 ng/μL/kbp) was injected into the pronucleus of fertilized eggs. The injected eggs were
419 transplanted into the oviduct ampulla of pseudopregnant mice (ICR; 10 embryos per
420 ampulla). After 19 days, pups were delivered through Caesarean section and placed
421 with foster mothers (ICR). For the rescue experiment, F0 Tg mice were mated with
422 *Trim41* KO mouse line. The mouse colony with the transgene and KO allele was
423 maintained by sibling mating. The genotyping primers (GeneDesign) are listed in Table
424 S1. The transgenic mouse line is available from Riken BRC (#11216) and CARD
425 (#3019).
426
427 ***Generation of ΔRING-Trim41 mice***
428 *ΔRING-Trim41* mice were generated by microinjection described previously
429 (Oura et al., 2020). First, a gRNA solution was prepared by annealing two tracrRNAs
430 (Sigma-Aldrich, St. Louis, MO, USA) and crRNA (Sigma-Aldrich). The target genomic
431 sequences are listed in Table S1. Then, the gRNA solution and Cas9 nuclease solution
432 (Thermo Fisher Scientific, Waltham, MA, USA) were mixed: 40 ng/μL gRNA each and
433 108 ng/μL Cas9 nucleases. The obtained complex was then microinjected into fertilized
434 eggs (B6D2F1) using a programmable microinjector (FemtoJet 4i, Eppendorf, Hamburg,
435 Germany). The microinjected eggs were then transplanted into the oviduct ampulla of
436 pseudopregnant mice (ICR) on the following day. After 19 days, pups were delivered
437 through Caesarean section and placed with foster mothers (ICR). To generate
438 heterozygous mutant mice, F0 mice were mated with WT B6D2F1. Mouse colonies with
439 the desired mutation were maintained by sibling mating. The genotyping primers
440 (GeneDesign) are listed in Table S1. The mutant mouse line is available from Riken

441 BRC (#11041) and CARD (#2948).

442

443 ***Bacterial strains***

444 *Escherichia coli* (*E. coli*) strain DH5α (Toyobo, Osaka, Japan) and BL21(de3)
445 pLysS (C606003, ThermoFisher Scientific) were used for DNA cloning and protein
446 expression, respectively. E. coli cells were grown in LB or 2×YT medium containing 100
447 mg/L ampicillin and were transformed or cloned using standard methods.

448

449 ***Production of anti-TRIM41 antibody***

450 Monoclonal antibody against TRIM41 was produced as previously described
451 (Oura et al., 2021). The DNA encoding mouse TRIM41 (residue 35-85 aa,
452 NP_663352.2) was inserted into pGEX6p-1 (GE healthcare), and the expression vector
453 was transformed into *E. coli* strain BL21 (de3) pLysS (C606003, Thermo Fisher
454 Scientific). GST-TRIM41 was purified using Glutathione Sepharose 4B (GE Healthcare).
455 The GST tag was removal by PreScission protease (27084301, GE Healthcare) and
456 Glutathione Sepharose 4B affinity subtraction purification. The purified TRIM41 protein
457 with a complete adjuvant was injected into female rats. After 17 days of injection,
458 lymphocytes were collected from iliac lymph nodes for hybridomas generation (Kishiro
459 et al., 1995; Sado et al., 2006). The hybridomas were cloned by a limited dilution and
460 screened by ELISA against recombinant TRIM41 and immunoblotting against testis
461 lysate. A monoclonal antibody from hybridoma clone #33-16 was used in this study. As a
462 side note, the #33-16 antibody also recognized ΔRING-TRIM41 missing 2-61 aa
463 residues, showing that the epitope of #33-16 is in 59-85 aa residues (two or three
464 mismatches might be acceptable).

465

466 ***Genotype analysis***

467 PCR was performed using KOD FX neo (KFX-201, TOYOBO). The primers
468 (GeneDesign) for each gene are summarized in Table S1. PCR products were purified
469 using a Wizard SV Gel and PCR Clean-Up System (Promega, Madison, WI, USA) kit
470 for Sanger sequencing.

471

472 ***Sequence comparison analysis***

473 Amino acid sequences of TRIM41 were obtained from the NCBI Entrez Protein
474 database. Clustal W2.1 was used for multiple sequence alignment (Larkin et al., 2007).

475

476 ***Immunoblotting***

477 Proteins from testis were extracted using NP40 lysis buffer [50mM Tris-HCl (pH
478 7.5), 150 mM NaCl, 0.5% NP-40, 10% Glycerol]. Proteins were separated by
479 SDS-PAGE under reducing conditions and transferred to polyvinylidene fluoride (PVDF)
480 membrane using the Trans Blot Turbo system (BioRad, Munich, Germany). After
481 blocking with 10% skim milk (232100, Becton Dickinson, Cockeysville, MD, USA), the
482 membrane was incubated with primary antibody overnight at 4°C, and then incubated
483 with HRP-conjugated secondary antibody for 1 h at room temperature.
484 Chemiluminescence was detected by ECL Prime Western Blotting Detection Reagents
485 (RPN2232, GE Healthcare, Chicago, IL, USA) using the Image Quant LAS 4000 mini
486 (GE Healthcare). The antibodies used in this study are listed in Table S2.

487

488 ***Fertility analysis***

To examine fertility, sexually mature male mice were caged with wild-type females (B6DF1) for at least three months. The vaginal plugs and pup's numbers were recorded at approximately 10 AM to determine the number of copulations and litter size. Numerical data is available in Table S3.

Morphological and histological analysis of testis and epididymis

To observe gross testis morphology and measure testicular weight, mice over 11-week-old age were euthanized after measuring their body weight. Numerical data is available in Table S3. The whole testis was observed using BX50 and SZX7 (Olympus, Tokyo, Japan) microscopes. For histological analysis, testes were fixed in Bouin's fixative solution (16045-1, Polysciences, Warrington, PA, USA) at 4°C O/N, dehydrated in increasing ethanol concentrations and 100% xylene, embedded in paraffin, and sectioned (5 µm). The paraffin sections were hydrated with 100% Xylene and decreasing ethanol concentrations, treated with 1% periodic acid (26605-32, Nacalai Tesque, Kyoto, Japan) for 10 min, incubated with Schiff's reagent (193-08445, Wako) for 20 min, counterstained with Mayer's hematoxylin solution (131-09665, Wako) for 3 min, dehydrated in increasing ethanol concentrations, and finally mounted with Permount (SP15-100-1, Ferma, Tokyo, Japan). The sections were observed using a BX53 (Olympus) microscope. Seminiferous tubule stages were identified based on the morphological characteristics of the germ cell nuclei (Ahmed and de Rooij, 2009).

Apoptosis detection in testicular section

TdT-mediated dUTP nick end labeling (TUNEL) staining was carried out with In Situ Apoptosis Detection Kit (MK500, Takara Bio Inc., Shiga, Japan), according to the

manufacturer's instruction. Briefly, testes were fixed with Bouin's fixative, embedded in paraffin, and sectioned (5 µm). After paraffin removal, the slides were boiled in citrate buffer (pH 6.0; 1:100; ab93678, abcam, Cambridge, UK) for 10 min and incubated in 3% H_2O_2 at room temperature for 5 min for endogenous peroxidase inactivation, followed by a labeling reaction with TdT enzyme and FITC-conjugated dUTP at 37°C for 1 h.

For chromogenic detection of apoptosis, the sections were incubated with HRP-conjugated anti-FITC antibody at 37°C for 30 min. The section was then incubated in ImmPACT DAB (SK-4105, Vector Laboratories, Burlingame, CA, USA) working solution, counterstained with Mayer's hematoxylin solution for 3 min, dehydrated in increasing ethanol concentrations, and finally mounted with Permount. The sections were observed using a BX53 (Olympus) microscope. Seminiferous tubule stages were identified based on the morphological characteristics of the germ cell nuclei (Ahmed and de Rooij, 2009). Numerical data is available in Table S3.

Immunostaining of surface chromosome spread

Spread nuclei from spermatocytes were prepared as previously described (Oji et al., 2020; Oura et al., 2021). Seminiferous tubules were unraveled using forceps in ice-cold DMEM (11995065, Thermo Fisher Scientific) and incubated in 1 mg/mL collagenase (C5138, Sigma-Aldrich) in DMEM (20 mL) at 37°C for 15 min. After three washes with DMEM, the tubules were transferred to 20 mL trypsin/DNaseI medium [0.025 w/v% trypsin, 0.01 w/v% EDTA, 10U DNase in DMEM] and incubated at 37 °C for 10 min. After adding 5 mL of heat-inactivated FCS and pipetting, the solution was filtered through a mesh (59 µm; N-N0270T, NBC Meshtec inc., Tokyo, Japan) to remove tubule debris. The collected testicular cells were resuspended in hypotonic solution [100

mM sucrose] and 10µL of the suspension was dropped onto a slide glass with 100 µL of fixative solution [1% PFA, 0.1% (v/v) Triton X-100]. The slides were then air-dried and washed with PBS containing 0.4% Photo-Flo 200 (1464510, Kodak Alaris, NY, USA) or frozen for longer storage at -80°C.

The spread samples were blocked with 10% goat serum in PBS and then incubated with primary antibodies overnight at 4°C in blocking solution. After incubation with AlexaFlour 488/546-conjugated secondary antibody (1:200) at room temperature for 1 h, samples are counterstained with Hoechst 33342 and mounted with Immu-Mount. The samples were observed using a BX53 (Olympus) microscope. The antibodies used in this study are listed in Table S2. Numerical data is available in Table S3.

Giemsa staining of metaphase I chromosome spreads

For preparing metaphase chromosome spreads, seminiferous tubules were unraveled using forceps in ice-cold PBS and transferred to a 1.5-mL tube with 1 mL of accutase (12679–54, Nacalai Tesque), followed by clipping the tubules, and a 5 min incubation at room temperature. After filtration with a mesh (59 µm; N-N0270T, NBC Meshtec inc.) and centrifugation, the cells were resuspended in 8 mL of hypotonic solution [1% sodium citrate] and incubated for 5 min at room temperature. The suspension was centrifuged and 7 mL of supernatant was aspirated. The cells were then resuspended in the remaining 1 mL of supernatant and 7 mL of Carnoy's Fixative [75% Methanol, 25% Acetic Acid] were added gradually while shaking. After 2 washes with Carnoy's Fixative, the cells were resuspended in ~ 0.5 mL of Carnoy's Fixative and dropped onto a wet glass slide. The slide was stained with Giemsa Stain Solution (079–04391, wako) and observed using a BX53 (Olympus) microscope.

561

562 ***Multicolor fluorescence in situ hybridization (mFISH) followed by SYCP3***
563 ***immunostaining***

564 Testicular germ cells were suspended in 3 mL of hypotonic solution [0.075%
565 potassium chrolide] and incubated for 20 min at room temperature. Then the cells were
566 mixed with 1 mL of Carnoy's Fixative [75% Methanol, 25% Acetic Acid] to the
567 suspension for fixing. After 5 mL of Carnoy's Fixative addition, the suspension was
568 again mixed and centrifuged at 1,500 rpm for 5 minutes. After three washes with 5 mL of
569 Carnoy's Fixative, the fixed cells were subjected to metaphase spreader Hanabi
570 (ADSTEC, Funabashi, Japan) for spread sample preparation.

571 For multicolor FISH analysis, the spread samples were hybridized with
572 21XMouse (MetaSystems, Altlussheim, Germany) according to the manufacturer's
573 protocol. For denaturation of the nuclear DNA, the spread samples were incubated in
574 2×SSC for 30 min at 70℃ and then treated with 0.07M NaOH for 1 min at room
575 temperature. The denatured samples were washed with 0.1×SSC and 2×SSC for 1 min
576 at 4℃, respectively, and then dehydrated with 70%, 95%, and 100% ethanol. Multicolor
577 FISH probes were denatured for 5 min at 75℃ and applied to the spread samples. After
578 hybridization for 48 h at 37℃ in a humidified chamber, the spread samples were treated
579 with 0.4× SSC for 2 min at 72℃, washed in 2×SSC containing 0.05% Tween20 for 30
580 sec at room temperature, and rinsed with distilled water.

581 Immunostaining of the spread nuclei with SYCP3 was performed described
582 above. After incubation of the spread samples with primary and secondary antibodies,
583 the slides were covered by a coverslip with DAPI/Antifade (MetaSystemes, Altlussheim,
584 Germany) and observed under a fluorescent microscope. Fluorescence images were

585 captured using a high-sensitive digital camera (α7s, SONY, Tokyo, Japan), and the
586 chromosome numbering of each synaptonemal complex was determined based on the
587 fluorescence color.
588
589 ***Immunoprecipitation***
590 Proteins from seminiferous tubules were extracted using NP40 lysis buffer [50
591 mM Tris-HCl (pH7.5), 150 mM NaCl, 0.5% NP-40, 10% Glycerol]. Protein lysates were
592 mixed with 20 μL Protein G-conjugated magnetic beads (DB10009, Thermo Fisher
593 Scientific) with 2.0 μg antibody. The immune complexes were incubated for 1 h at 4°C
594 and washed 3 times with NP40 lysis buffer. Co-immunoprecipitated products were then
595 eluted by resuspension in 2x SDS sample buffer [125 mM Tris-HCl (pH6.8), 10%
596 2-mercaptoethanol, 4% sodium dodecyl sulfate (SDS), 10% sucrose, 0.01%
597 bromophenol blue] and 10 min incubation at 70°C. The antibodies used in this study are
598 listed in Table S2.
599
600 ***Mass spectrometry and data analysis.***
601 Before MS analysis, half of the eluted amount was subjected to SDS-PAGE
602 and silver staining (06865-81, Nacalai Tesque). The remaining half amount was
603 subjected to mass spectrometry (MS) analysis. The proteins were reduced with 10 mM
604 dithiothreitol (DTT), followed by alkylation with 55 mM iodoacetamide, and digested by
605 treatment with trypsin and purified with a C18 tip (GL-Science, Tokyo, Japan). The
606 resultant peptides were subjected to nanocapillary reversed-phase LC-MS/MS analysis
607 using a C18 column (25 cm × 75 um, 1.6 μm; IonOpticks, Victoria, Australia) on a
608 nanoLC system (Bruker Daltoniks, Bremen, Germany) connected to a tims TOF Pro

609 mass spectrometer (Bruker Daltoniks) and a modified nano-electrospray ion source
610 (CaptiveSpray; Bruker Daltoniks). The mobile phase consisted of water containing 0.1%
611 formic acid (solvent A) and acetonitrile containing 0.1% formic acid (solvent B). Linear
612 gradient elution was carried out from 2% to 35% solvent B for 18 min at a flow rate of
613 400 nL/min. The ion spray voltage was set at 1.6 kV in the positive ion mode. Ions were
614 collected in the trapped ion mobility spectrometry (TIMS) device over 100 ms and MS
615 and MS/MS data were acquired over an *m/z* range of 100-1,700. During the collection of
616 MS/MS data, the TIMS cycle was adjusted to 1.1 s and included 1 MS plus 10 parallel
617 accumulation serial fragmentation (PASEF)-MS/MS scans, each containing on average
618 12 MS/MS spectra (>100 Hz), and nitrogen gas was used as the collision gas.

619 The resulting data were processed using DataAnalysis version 5.1 (Bruker
620 Daltoniks), and proteins were identified using MASCOT version 2.6.2 (Matrix Science,
621 London, UK) against the SwissProt database. Quantitative value (available in Table S4)
622 and fold exchange were calculated by Scaffold4 (Proteome Software, Portland, OR,
623 USA) for MS/MS-based proteomic studies.

624

625 ***Statistics and Reproducibility***

626 All error bars indicated standard deviation. The sample numbers were
627 described in each legend or/and in the figure panel.

Acknowledgments

We wish to thank the members of both the Department of Experimental Genome Research, Animal Resource Center for Infectious Diseases, and NPO for Biotechnology Research and Development for experimental assistance. We also thank Dr. Kusakabe and Dr. Tateno at Department of Biological Sciences, Asahikawa Medical University for technical consultation of mFISH experiments.

Competing interests

The authors declare no competing interests.

Fundings

This work was supported by: the Japan Society for the Promotion of Science (JSPS) KAKENHI grants (JP19J21619 to S.O., JP19H05758 to T.H., JP18K14612 and JP20H03172 to T.N., and JP19H05750 and 21H04753 to M.I.); Japan Agency for Medical Research and Development (AMED) grants (JP20gm5010001 to M.I.); Takeda Science Foundation Grants to T.N. and M.I.; The Nakajima Foundation to T.N.; and the Bill & Melinda Gates Foundation (INV-001902 to M.I.).

Data availability

The authors declare that the data supporting this study's findings are available from the corresponding author upon request. Numerical data that underlies graphs were listed in Table S3.

References

Ahmed, E. A. and de Rooij, D. G. (2009). Staging of mouse seminiferous tubule cross-sections. *Methods in molecular biology (Clifton, N.J.)* **558**, 263-277.

Boateng, K. A., Bellani, M. A., Gregoretti, I. V., Pratto, F. and Camerini-Otero, R. D. (2013). Homologous pairing preceding SPO11-mediated double-strand breaks in mice. *Developmental cell* **24**, 196-205.

Federici, F., Mulugeta, E., Schoenmakers, S., Wassenaar, E., Hoogerbrugge, J. W., van der Heijden, G. W., van Cappellen, W. A., Slotman, J. A., van, I. W. F., Laven, J. S., et al. (2015). Incomplete meiotic sex chromosome inactivation in the domestic dog. *BMC genomics* **16**, 291.

Fujihara, Y., Kaseda, K., Inoue, N., Ikawa, M. and Okabe, M. (2013). Production of mouse pups from germline transmission-failed knockout chimeras. *Transgenic research* **22**, 195-200.

Fujiwara, Y., Horisawa-Takada, Y., Inoue, E., Tani, N., Shibuya, H., Fujimura, S., Kariyazono, R., Sakata, T., Ohta, K., Araki, K., et al. (2020). Meiotic cohesins mediate initial loading of HORMAD1 to the chromosomes and coordinate SC formation during meiotic prophase. *PLoS genetics* **16**, e1009048.

Gray, S. and Cohen, P. E. (2016). Control of Meiotic Crossovers: From Double-Strand Break Formation to Designation. *Annual review of genetics* **50**, 175-210.

Hatakeyama, S. (2017). TRIM Family Proteins: Roles in Autophagy, Immunity, and Carcinogenesis. *Trends in biochemical sciences* **42**, 297-311.

Hermann, B. P., Cheng, K., Singh, A., Roa-De La Cruz, L., Mutoji, K. N., Chen, I. C., Gildersleeve, H., Lehle, J. D., Mayo, M., Westernströer, B., et al. (2018). The Mammalian Spermatogenesis Single-Cell Transcriptome, from Spermatogonial Stem Cells to Spermatids. *Cell reports* **25**, 1650-1667.e1658.

Ikawa, M., Nakanishi, T., Yamada, S., Wada, I., Kominami, K., Tanaka, H., Nozaki, M., Nishimune, Y. and Okabe, M. (2001). Calmegin is required for fertilin alpha/beta heterodimerization and sperm fertility. *Developmental biology* **240**, 254-261.

Ishiguro, K., Kim, J., Fujiyama-Nakamura, S., Kato, S. and Watanabe, Y. (2011). A new meiosis-specific cohesin complex implicated in the cohesin code for homologous pairing. *EMBO reports* **12**, 267-275.

Ishiguro, K., Kim, J., Shibuya, H., Hernández-Hernández, A., Suzuki, A., Fukagawa, T., Shioi, G., Kiyonari, H., Li, X. C., Schimenti, J., et al. (2014). Meiosis-specific cohesin mediates homolog recognition in mouse spermatocytes. *Genes & development* **28**, 594-607.

686 **Ishiguro, K. and Watanabe, Y.** (2016). The cohesin REC8 prevents illegitimate inter-sister
687 synaptonemal complex assembly. *EMBO reports* **17**, 783-784.
688 **Ishiguro, K. I.** (2019). The cohesin complex in mammalian meiosis. *Genes to cells : devoted*
689 *to molecular & cellular mechanisms* **24**, 6-30.
690 **Keeney, S., Lange, J. and Mohibullah, N.** (2014). Self-organization of meiotic
691 recombination initiation: general principles and molecular pathways. *Annual*
692 *review of genetics* **48**, 187-214.
693 **Kim, D. I., Jensen, S. C., Noble, K. A., Kc, B., Roux, K. H., Motamedchaboki, K. and Roux,**
694 **K. J.** (2016). An improved smaller biotin ligase for BioID proximity labeling.
695 *Molecular biology of the cell* **27**, 1188-1196.
696 **Kim, J., Ishiguro, K., Nambu, A., Akiyoshi, B., Yokobayashi, S., Kagami, A., Ishiguro,**
697 **T., Pendas, A. M., Takeda, N., Sakakibara, Y., et al.** (2015). Meikin is a conserved
698 regulator of meiosis-I-specific kinetochore function. *Nature* **517**, 466-471.
699 **Kishiro, Y., Kagawa, M., Naito, I. and Sado, Y.** (1995). A novel method of preparing
700 rat-monoclonal antibody-producing hybridomas by using rat medial iliac lymph node
701 cells. *Cell structure and function* **20**, 151-156.
702 **Larkin, M. A., Blackshields, G., Brown, N. P., Chenna, R., McGettigan, P. A., McWilliam,**
703 **H., Valentin, F., Wallace, I. M., Wilm, A., Lopez, R., et al.** (2007). Clustal W
704 and Clustal X version 2.0. *Bioinformatics (Oxford, England)* **23**, 2947-2948.
705 **Lassot, I., Mora, S., Lesage, S., Zieba, B. A., Coque, E., Condroyer, C., Bossowski, J.**
706 **P., Mojsa, B., Marelli, C., Soulet, C., et al.** (2018). The E3 Ubiquitin Ligases
707 TRIM17 and TRIM41 Modulate α-Synuclein Expression by Regulating ZSCAN21. *Cell*
708 *reports* **25**, 2484-2496.e2489.
709 **Liu, J. G., Yuan, L., Brundell, E., Björkroth, B., Daneholt, B. and Höög, C.** (1996).
710 Localization of the N-terminus of SCP1 to the central element of the synaptonemal
711 complex and evidence for direct interactions between the N-termini of SCP1
712 molecules organized head-to-head. *Experimental cell research* **226**, 11-19.
713 **Meuwissen, R. L., Offenberg, H. H., Dietrich, A. J., Riesewijk, A., van Iersel, M. and**
714 **Heyting, C.** (1992). A coiled-coil related protein specific for synapsed regions
715 of meiotic prophase chromosomes. *The EMBO journal* **11**, 5091-5100.
716 **Niu, W. and Spradling, A. C.** (2020). Two distinct pathways of pregranulosa cell
717 differentiation support follicle formation in the mouse ovary. *Proceedings of the*
718 *National Academy of Sciences of the United States of America* **117**, 20015-20026.
719 **Oji, A., Isotani, A., Fujihara, Y., Castaneda, J. M., Oura, S. and Ikawa, M.** (2020). Tesmin,
720 Metallothionein-Like 5, is Required for Spermatogenesis in Mice†. *Biology of*
721 *reproduction* **102**, 975-983.

Oura, S., Kazi, S., Savolainen, A., Nozawa, K., Castañeda, J., Yu, Z., Miyata, H., Matzuk, R. M., Hansen, J. N., Wachten, D., et al. (2020). Cfap97d1 is important for flagellar axoneme maintenance and male mouse fertility. *PLoS genetics* **16**, e1008954.

Oura, S., Koyano, T., Kodera, C., Horisawa-Takada, Y., Matsuyama, M., Ishiguro, K. I. and Ikawa, M. (2021). KCTD19 and its associated protein ZFP541 are independently essential for meiosis in male mice. *PLoS genetics* **17**, e1009412.

Ozato, K., Shin, D. M., Chang, T. H. and Morse, H. C., 3rd (2008). TRIM family proteins and their emerging roles in innate immunity. *Nature reviews. Immunology* **8**, 849-860.

Patil, G., Xu, L., Wu, Y., Song, K., Hao, W., Hua, F., Wang, L. and Li, S. (2020). TRIM41-Mediated Ubiquitination of Nucleoprotein Limits Vesicular Stomatitis Virus Infection. *Viruses* **12**.

Patil, G., Zhao, M., Song, K., Hao, W., Bouchereau, D., Wang, L. and Li, S. (2018). TRIM41-Mediated Ubiquitination of Nucleoprotein Limits Influenza A Virus Infection. *Journal of virology* **92**.

Rajsbaum, R., García-Sastre, A. and Versteeg, G. A. (2014). TRIMmunity: the roles of the TRIM E3-ubiquitin ligase family in innate antiviral immunity. *Journal of molecular biology* **426**, 1265-1284.

Roux, K. J., Kim, D. I., Raida, M. and Burke, B. (2012). A promiscuous biotin ligase fusion protein identifies proximal and interacting proteins in mammalian cells. *The Journal of cell biology* **196**, 801-810.

Sado, Y., Inoue, S., Tomono, Y. and Omori, H. (2006). Lymphocytes from enlarged iliac lymph nodes as fusion partners for the production of monoclonal antibodies after a single tail base immunization attempt. *Acta histochemica et cytochemica* **39**, 89-94.

Scully, R., Chen, J., Plug, A., Xiao, Y., Weaver, D., Feunteun, J., Ashley, T. and Livingston, D. M. (1997). Association of BRCA1 with Rad51 in mitotic and meiotic cells. *Cell* **88**, 265-275.

Trinkle-Mulcahy, L. (2019). Recent advances in proximity-based labeling methods for interactome mapping. *F1000Research* **8**.

Versteeg, G. A., Rajsbaum, R., Sánchez-Aparicio, M. T., Maestre, A. M., Valdiviezo, J., Shi, M., Inn, K. S., Fernandez-Sesma, A., Jung, J. and García-Sastre, A. (2013). The E3-ligase TRIM family of proteins regulates signaling pathways triggered by innate immune pattern-recognition receptors. *Immunity* **38**, 384-398.

Watanabe, D., Okabe, M., Hamajima, N., Morita, T., Nishina, Y. and Nishimune, Y. (1995). Characterization of the testis-specific gene 'calmegin' promoter sequence and its

activity defined by transgenic mouse experiments. *FEBS letters* **368**, 509-512.

Woods, L. M., Hodges, C. A., Baart, E., Baker, S. M., Liskay, M. and Hunt, P. A. (1999). Chromosomal influence on meiotic spindle assembly: abnormal meiosis I in female Mlh1 mutant mice. *The Journal of cell biology* **145**, 1395-1406.

Xu, H., Beasley, M. D., Warren, W. D., van der Horst, G. T. and McKay, M. J. (2005). Absence of mouse REC8 cohesin promotes synapsis of sister chromatids in meiosis. *Developmental cell* **8**, 949-961.

Yu, Z., Li, X., Yang, M., Huang, J., Fang, Q., Jia, J., Li, Z., Gu, Y., Chen, T. and Cao, X. (2021). TRIM41 is required to innate antiviral response by polyubiquitinating BCL10 and recruiting NEMO. *Signal transduction and targeted therapy* **6**, 90.

Zhang, S., Guo, J. T., Wu, J. Z. and Yang, G. (2013). Identification and characterization of multiple TRIM proteins that inhibit hepatitis B virus transcription. *PloS one* **8**, e70001.

Zhang, X., Hu, Z., Wang, X., Li, L., Zhu, B., Lin, X., Zhang, J. and Hua, Z. (2021). ANXA10 promotes melanoma metastasis by suppressing E3 ligase TRIM41-directed PKD1 degradation. *Cancer letters* **519**, 237-249.

Figure legends

Fig. 1: Production of *Trim41* KO mice and fertility analysis.

(A) Schematic of TRIM41 protein structure and antigen position. (B) Model of TRIM E3 ubiquitin ligase activity. The RING domain at the N terminus interacts with E2 ubiquitin-conjugating enzyme. The C terminal part of TRIM recognizes the substrates. (C) Phylogenetic tree constructed by ClustalW with TRIM41 sequences of various mammals. (D) RT-PCR using multi-tissue cDNA. *Actb* was used as a loading control. (E) RT-PCR using postnatal testis cDNA. (F) RT-PCR using embryonic ovary cDNA. (G) Targeting scheme for *Trim41* disruption and a Tg contract. Black and white boxes in the gene map indicate coding and non-coding regions, respectively. Black arrowheads (Primer F1, F2, R1, R2, and R3) indicate primers for genotyping. (H) An example of genotyping PCR with primer sets in G. (I) The result of mating tests. Pups/plug: 8.9±1.7 [Het]; 0 [KO]; 9.4±2 [KO-Tg] (s.d.). Error bars indicate standard deviation. The numerical data is available in Table S3. (J) Pup numbers from mating pairs of *Trim41* KO females and *Trim41* Het males (7.4±2.3; s.d.). Error bars indicate standard deviation. The numerical data is available in Table S3.

Fig. 2: Histological analysis of *Trim41* KO male mice.

(A and B) Testis morphology (A) and testis/bodyweight of WT, *Trim41* Het**,** *Trim41* KO, and KO-Tg adult mice (B). Testis/body weight: 3.2±0.3 x 10−3 [WT], 3.1±0.2 x 10−3 [Het] , 1.2±0.2 x 10^{-3} [KO], 2.8±0.1 x 10^{-3} [KO-Tg]. Error bars indicate standard deviation. The numerical data is available in Table S3. (C) PAS staining of seminiferous tubules of adult mice. The seminiferous epithelium cycle was determined by germ cell position and nuclear morphology. Red arrows indicate elongated spermatids with

799 abnormal head morphology. At least three male mice were analyzed. (D) TUNEL
800 staining of seminiferous tubules of adult mice counterstained with hematoxylin. At least
801 three male mice were analyzed. (E) The stacked bar graph of TUNEL positive cells. The
802 seminiferous epithelial stages were roughly determined by the arrangement and nuclear
803 morphology of the first layer of germ cells (spermatogonia and leptotene/zygotene
804 spermatocytes). The numerical data is available in Table S3. (F) PAS staining of cauda
805 epididymis of adult mice. At least three male mice were analyzed. (G) Spermatozoa
806 extracted from cauda epididymis of adult mice.
807
808 **Fig. 3: Cytological analysis of *Trim41* KO spermatocytes.**
809 (A and B) Immunostaining of spread nuclei from prophase spermatocytes collected from
810 adult Het (A) and KO (B) male mice. White arrows indicate overloaded SYCP3 axes. At
811 least three male mice were analyzed. (C) Additional immunostaining images of KO
812 spermatocytes. The yellow arrowhead indicates the X chromosome with two SYCP3
813 axes. The red arrowhead shows the evident synapsis between the sex chromosome
814 and autosomes (only 17 axes existed outside the γH2AX cloud). (D) The percentage of
815 each meiotic prophase stage in immunostained spread nuclei samples in A and B. The
816 numerical data is available in Table S3. (E) Immunostaining of metaphase and
817 anaphase spermatocytes squashed from seminiferous tubules after fixation. Magenta
818 and blue arrowheads indicate polycomplex-like structures, aggregate of SYCP3, and
819 chromosomes connected with the polycomplex-like structures. At least three male mice
820 were analyzed. (F) Giemsa staining of spread nuclei of metaphase I spermatocytes.
821 Black arrows indicate the miscondensation of chromosomes. At least three male mice
822 were analyzed. (G) Multicolor FISH followed by SYCP3 immunostaining. White arrows

823 indicate overloaded SYCP3 axes. (H) The histogram for the chromosome distribution of
824 SYCP3 overloaded axes. Forty-three well-spread cells were analyzed.
825
826 **Fig. 4: Synapsis configuration of SYCP3 overloaded axes.**
827 (A and B) SYCP1 immunostaining of spread nuclei from prophase spermatocytes
828 collected from adult Het (A) and KO (B) male mice. The sex chromosomes were
829 identified by their characteristic shape of SYCP3 axes. At least three male mice were
830 analyzed. (C and D) BRCA1 immunostaining of spread nuclei from prophase
831 spermatocytes collected from adult Het (C) and KO (D) male mice. At least three male
832 mice were analyzed.
833
834 **Fig. 5: Production and phenotypical analysis of *Trim41*$^{\Delta RING/\Delta RING}$ mice.**
835 (A) Knock-in scheme for the replacement of the RING domain with HA tag. Black and
836 white boxes in the gene map indicate coding and non-coding regions, respectively.
837 Black arrowheads (F3 and R4) and arrows (gRNA1 and gRNA2) indicate primers for
838 genotyping and target sequence of gRNAs, respectively. (B) An example of genotyping
839 PCR with primer sets in A. (C and D) Immunoblotting analysis with anti-HA (C) and
840 -TRIM41 (D) antibodies. Black and red arrows indicate TRIM41 and HA-ΔRING-TRIM41,
841 respectively. (E) The result of mating tests. Pups/plug: 9.1±2.5 [WT]; 0 [ΔR-Homo] (s.d.).
842 Error bars indicate standard deviation. The numerical data is available in Table S3. (F
843 and G) Testis morphology (F) and testis/bodyweight of ΔR-Het and ΔR-Homo adult mice
844 (G). Testis/body weight: 3.6±0.0 x 10^{-3} [ΔR-Het]; 1.5±0.2 x 10^{-3} [ΔR-Homo]. Error bars
845 indicate standard deviation. The numerical data is available in Table S3. (H) PAS
846 staining of seminiferous tubules of adult mice. The seminiferous epithelium cycle was

847 determined by germ cell position and nuclear morphology. At least three male mice
848 were analyzed. (I) TUNEL staining of seminiferous tubules of adult mice counterstained
849 with hematoxylin. At least three male mice were analyzed. (J) The stacked bar graph of
850 TUNEL positive cells. The seminiferous epithelial stages were roughly determined by
851 the arrangement and nuclear morphology of the first layer of germ cells (spermatogonia
852 and leptotene/zygotene spermatocytes). The numerical data is available in Table S3.
853 (K) PAS staining of cauda epididymis of adult mice. At least three male mice were
854 analyzed.
855
856 **Fig. 6: Cytological analysis of *Trim41*$^{\Delta RING/\Delta RING}$ spermatocytes.**
857 (A and B) SYCP3/γH2AX immunostaining of pachytene spermatocytes from ΔR-Het (A)
858 and ΔR-Homo (B) male mice. At least three male mice were analyzed. (C–F) SYCP3/HA
859 immunostaining of pachytene spermatocytes from ΔR-Het (C), ΔR-Homo (D), *Trim41*$^{neo/\Delta RING}$
860 (E), and KO (F) male mice. White and blue arrowheads indicate HA signals on and
861 outside of SYCP3 axes, respectively. At least three male mice were analyzed for ΔR-Het
862 and ΔR-Homo. (G) SYCP1/HA immunostaining of surface chromosome spread from
863 ΔR-Homo testis. Magenta and yellow arrowheads indicate HA signals on the SYCP1
864 positive/negative boundary and the non-homologous axis interface, respectively. At
865 least three male mice were analyzed. (H) BRCA1/HA immunostaining of surface
866 chromosome spread from ΔR-Homo testis. Red arrowheads indicate HA signals on the
867 BRCA1 negative part of the X chromosome axes. At least three male mice were
868 analyzed.

Supplemental information

Fig. S1: *Trim41* is an evolutionally conserved gene expressed highly in pachytene germ cells.

(A) The percentage of TF342569 annotated species based on TreeFam database (Release 9; http://www.treefam.org/). Dark and light green show species with and without TF342569 annotation, respectively. (B) Protein sequence comparison of TRIM41 in big brown bat (XP_027991236.1), cat (XP_003980687.1), cattle (NP_001193094.1), chimpanzee (XP_016809993.1), dog (XP_038536985.1), human (NP_291027.3), mouse (NP_663352.2), pig (XP_020939058.1), and rat (NP_001128209.1). (C) The *Trim41* expression profile between testicular cells based on published single-cell RNA sequencing data, visualized by 10 x genomics Loupe Browser. UMI means Unique Molecular Identifiers. (D) The *Trim41* expression profile between embryonic female germ cells based on published single-cell RNA sequencing data.

Fig. S2: Expression confirmation of *Clgn-Trim41 Tg*

(A) RT-PCR using postnatal testis of *Trim41* KO-Tg male mice. (B) Immunoblotting analysis with an anti-PA antibody. RT means reverse transcription. The black arrow indicates a specific band in Tg. (C) Immunoblotting analysis with an anti-TRIM41 antibody raised against a recombinant TRIM41 protein (35-85 amino acid residues). The black and red arrows indicate a specific band in Tg and WT, respectively.

Fig. S3: Immunostaining of zygotene–pachytene spermatocytes, related to Fig 3A-C.

(A and B) Additional immunostaining images of zygotene–pachytene spermatocytes

893 from Het (A) and KO (B) male mice. The white dashed line shows nuclei of different
894 cells. The white arrowhead indicates SYCP3 overloading. The images were arranged in
895 the order of meiotic progression from the zygotene stage (top) to the early pachytene
896 stage (bottom).
897
898 **Fig. S4: Immunostaining of meiotic cohesins.**
899 (A and B) SYCP3/REC8 immunostaining of spread nuclei from prophase spermatocytes
900 collected from adult WT (A) and KO (B) male mice. (C and D) SYCP3/RAD21L
901 immunostaining of spread nuclei from prophase spermatocytes collected from adult WT
902 (A) and KO (B) male mice.
903
904 **Fig. S5: Phenotypical analysis of *Trim41* KO females**
905 (A) Gross morphology of female gonads from E15.5 fetus. (B) Immunostaining of female
906 gonad sections. White arrows indicate intense SYCP3 signals. (C) Ovarian histology of
907 *Trim41* Het and KO females. The ovaries were collected 10 h after intraperitoneal
908 administration of hCG.
909
910 **Fig. S6: Immunostaining of prophase I spermatocytes, related to Fig 6A and B.**
911 (A and B) Immunostaining of spread nuclei from prophase spermatocytes collected from
912 adult ΔR-Het (A) and ΔR-Homo (B) male mice. At least three male mice were analyzed.
913 (C) The percentage of each meiotic prophase stage in immunostained spread nuclei
914 samples in A and B. The numerical data is available in Table S3.
915
916 **Fig. S7: Additional images for ΔRING-TRIM41 accumulation, related to Fig 6C-F.**

(A) SYCP3/HA immunostaining of zygotene–diplotene spermatocytes from) ΔR-Homo male mice. White and blue arrowheads indicate HA signals on and outside of SYCP3 axes, respectively. At least three male mice were analyzed. (B–E) SYCP3/TRIM41 immunostaining of pachytene spermatocytes from Het (B), KO (C), ΔR-Het (D), and ΔR-Homo (E) male mice. White arrowheads indicate HA signals on SYCP3 axes. At least three male mice were analyzed.

Fig. S8: Additional images for SYCP1 and BRCA1 immunostaining, related to Fig 6G and H.

(A) SYCP1/HA immunostaining of surface chromosome spread from ΔR-Homo testis. Magenta and yellow arrowheads indicate HA signals on the SYCP1 positive/negative boundary and the non-homologous axis interface, respectively. At least three male mice were analyzed. (B) BRCA1/HA immunostaining of surface chromosome spread from ΔR-Homo testis. Red arrowheads indicate HA signals on the BRCA1 negative part of the X chromosome axes. At least three male mice were analyzed.

Fig. S9: Immunoprecipitation for substrate identification.

(A and B) Immunoprecipitation using an anti-TRIM41 antibody and WT testis lysate. TRIM41 immunoblotting (A) validated the immunoprecipitation capability of the anti-TRIM41 antibody and the success of immunoprecipitation experiments. Red and green arrowheads indicate TRIM41 and SYCP3, respectively. (C and D) Immunoprecipitation using an anti-TRIM41 antibody and ΔR-Homo testis lysate. HA immunoblotting (C) validated the success of immunoprecipitation experiments. Black and green arrowheads indicate HA-ΔRING-TRIM41 and SYCP3, respectively. (E and F)

941 Immunoprecipitation using an anti-HA antibody and ΔR-Homo testis lysate. HA
942 immunoblotting (E) validated the success of immunoprecipitation experiments. Black
943 and green arrowheads indicate HA-ΔRING-TRIM41 and SYCP3, respectively. (G and
944 H) Mass analysis of co-IPed elutes using anti-TRIM41 (G) and anti-HA (H) antibodies.
945 Proteins with 0 spectra in KO lysate were extracted and summarized in the table. The
946 whole proteomics data are available in Table S4. (I) Proteins detected more than twice
947 in G and H were summarized.
948
949 **Table. S1: Primers and gRNAs used in this study.**
950
951 **Table. S2: Antibodies used in this study.**
952
953 **Table. S3: Numerical data that underlies graphs.**
954
955 **Table. S4: The quantitative value of mass spectrometry analysis.**
956

Figure1

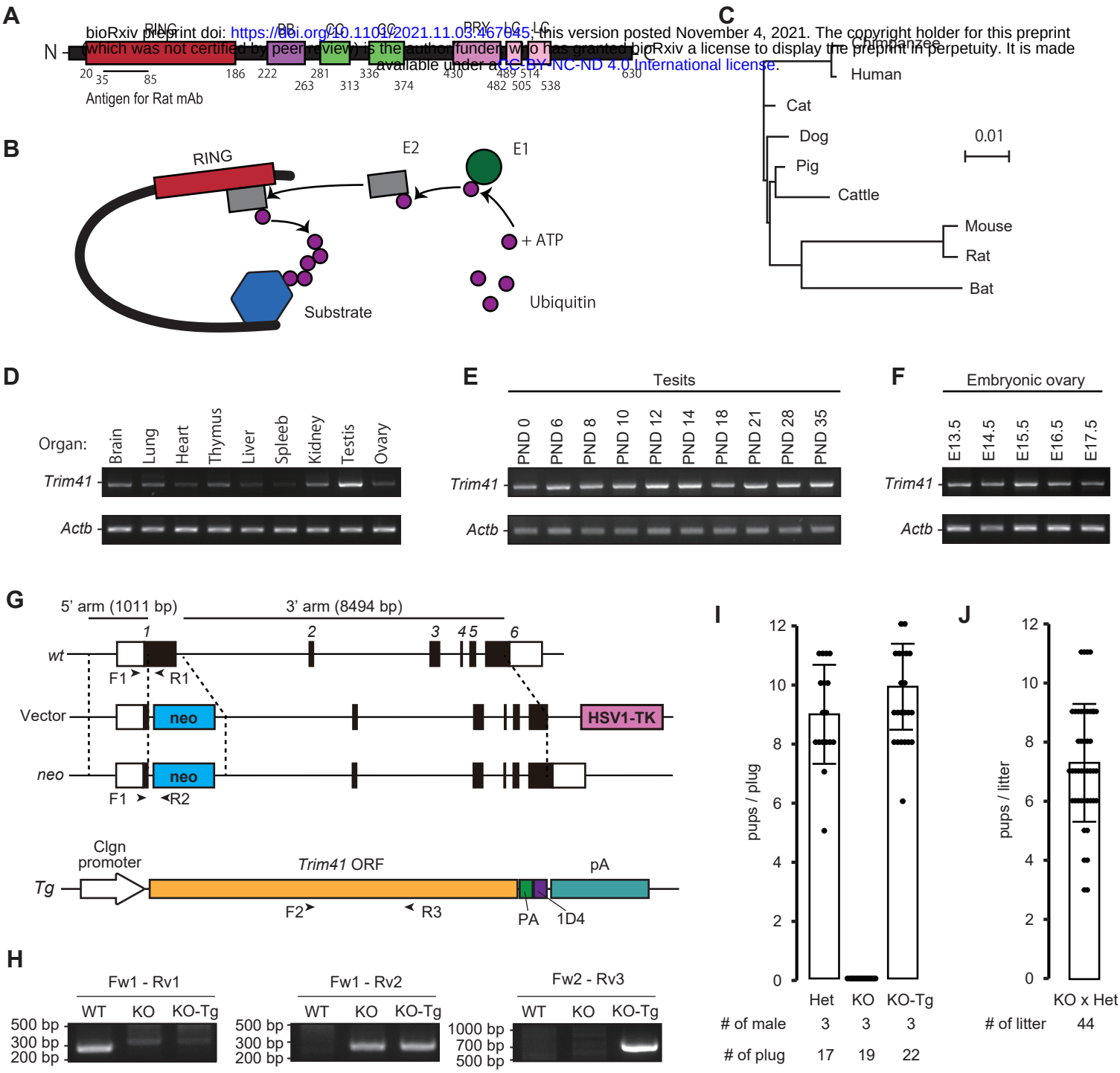

Figure2

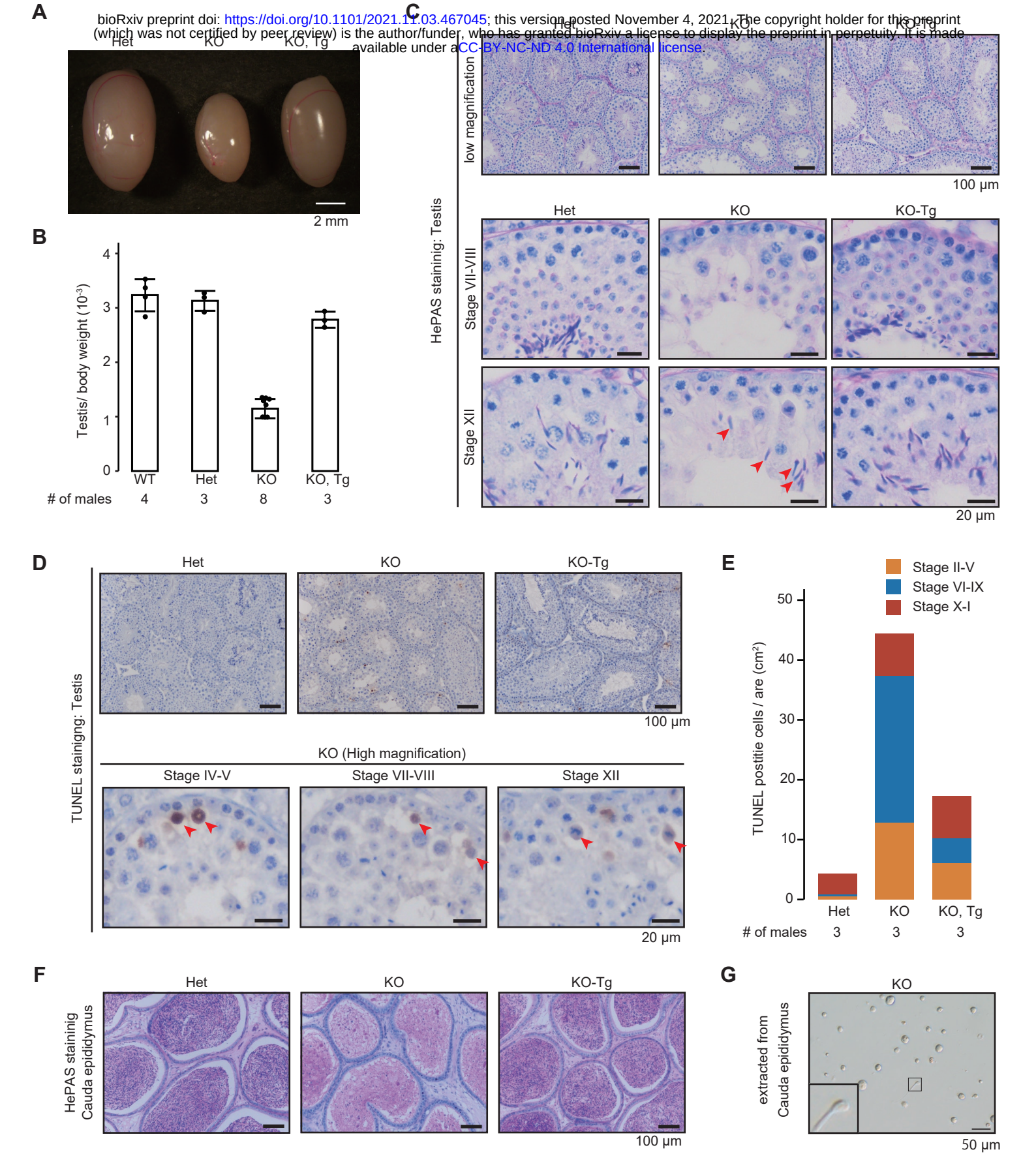

Figure 3

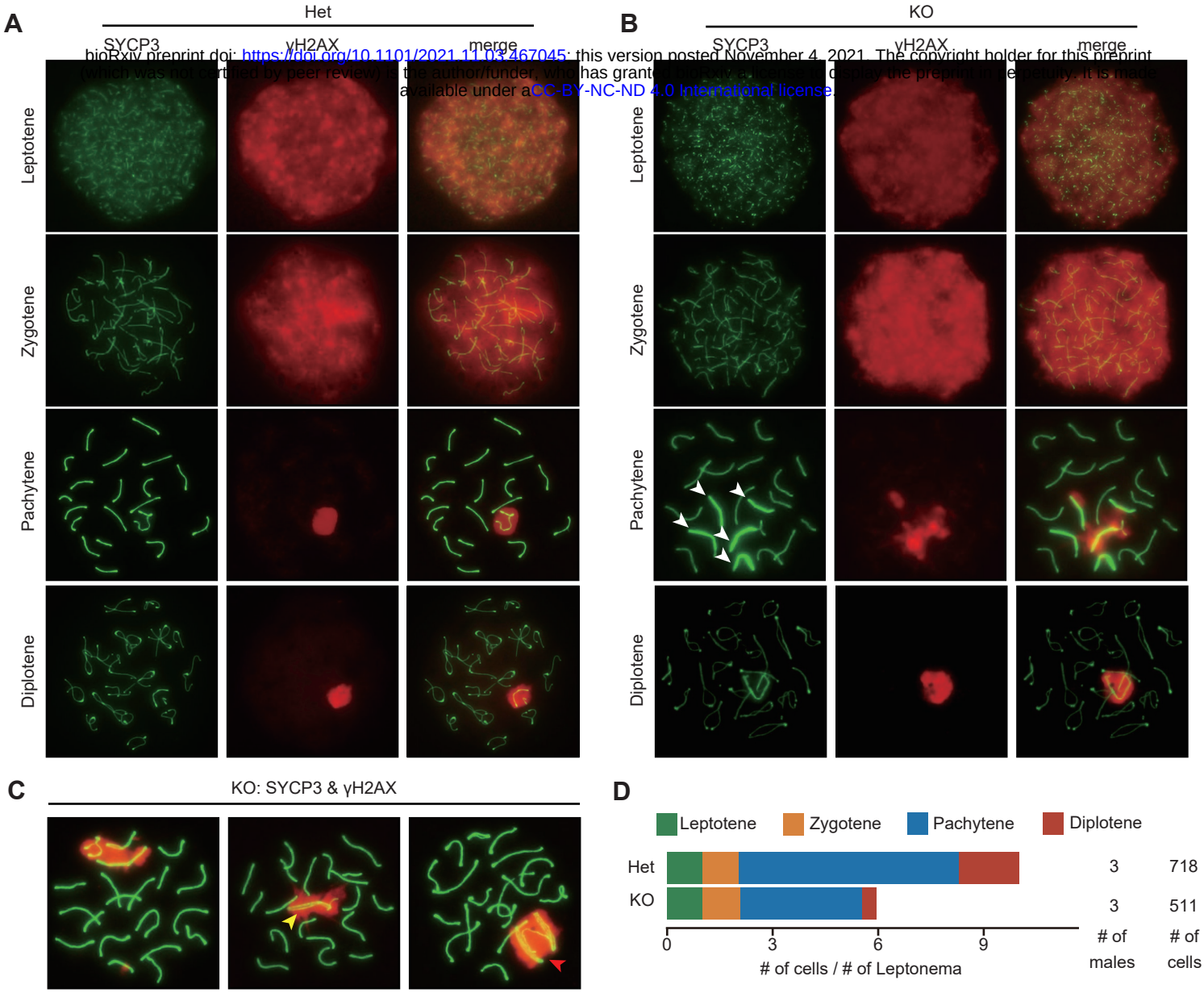

Figure4

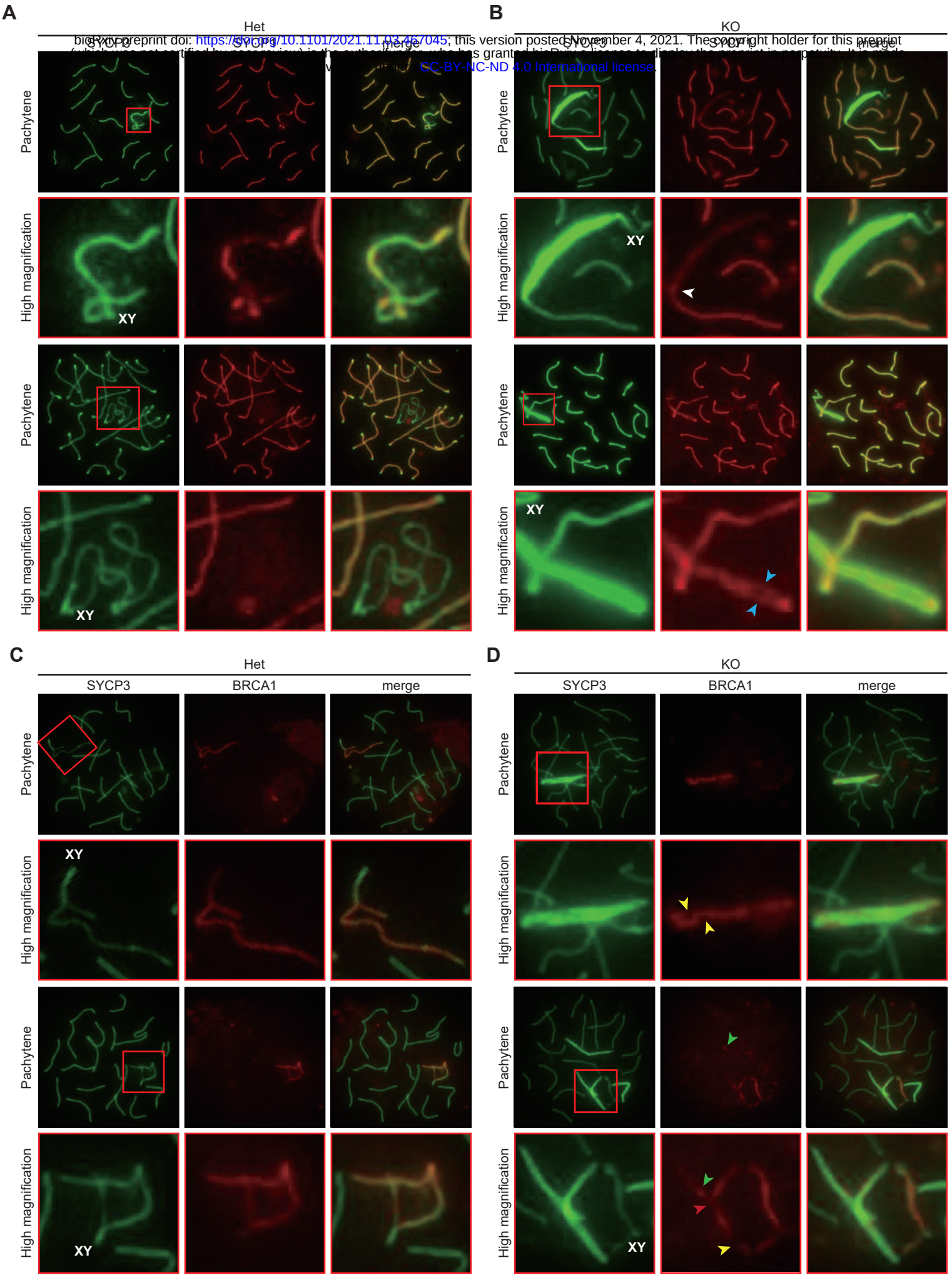

Figure5

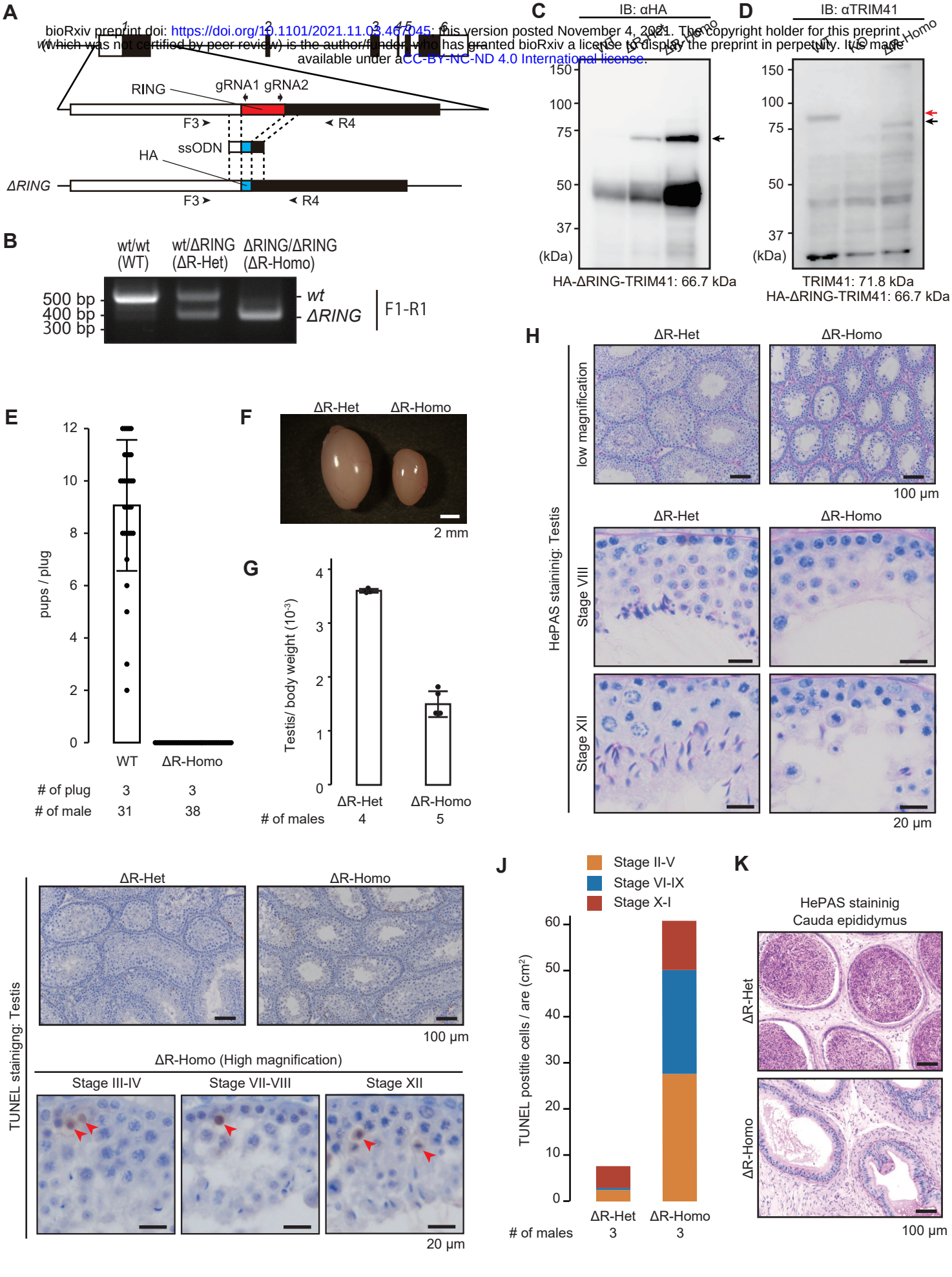

Figure 6